Comparison of point detection and area detection for point-scanning structured illumination microscopy

Wenshuai Wu*, Jiajie Chen*,‡, Meiting Wang*, Lei Wang*, Xiaomin Zheng*,
Jia Li*, Junle Qu*, Bruce Zhi Gao† and Yonghong Shao*,§

*College of Physics and Optoelectronic Engineering
Key Laboratory of Optoelectronic Devices
and Systems of Ministry of Education and Guangdong Province
Shenzhen University, Shenzhen 518060, Guangdong, P. R. China

†Department of Bioengineering and COMSET
Clemson University, Clemson, SC 29634 USA
‡cjj@szu.edu.cn
§shaoyh@szu.edu.cn

Structured illumination microscopy (SIM) is suitable for biological samples because of its relatively low-peak illumination intensity requirement and high imaging speed. The system resolution is affected by two typical detection modes: Point detection and area detection. However, a systematic analysis of the imaging performance of the different detection modes of the system has rarely been conducted. In this study, we compared laser point scanning point detection (PS-PD) and point scanning area detection (PS-AD) imaging in nonconfocal microscopy through theoretical analysis and simulated imaging. The results revealed that the imaging resolutions of PS-PD and PS-AD depend on excitation and emission point spread functions (PSFs), respectively. Especially, we combined the second harmonic generation (SHG) of point detection (P-SHG) and area detection (A-SHG) with SIM to realize a nonlinear SIM-imaging technique that improves the imaging resolution. Moreover, we analytically and experimentally compared the nonlinear SIM performance of P-SHG with that of A-SHG.

Keywords: Super-resolution; structured illumination microscopy; second harmonic generation.

1. Introduction

A series of super-resolution optical microscope imaging techniques have been developed in recent years to observe the diffraction-limited and ultrafine structures of bio-samples. These are divided into three categories.

‡,§Corresponding authors.

The first category is super-resolution microscopy, which is based on the single-molecule localization imaging principle.[1] A super-resolution image is reconstructed by obtaining the position of each fluorescent molecule through multiple imaging and computational localization. Techniques that use this method to achieve super-resolution imaging include fluorescence photoactivation localization microscopy,[1] stochastic optical reconstruction microscopy,[2] and photoactivated localization microscopy.[3] Single-molecule localization-based super-resolution microscopic imaging can acquire images with a resolution range of 10–30 nm, and it does not require an intense excitation light.[4,5] However, the type of technique is time-consuming, processes large volumes of data, and requires specific fluorescent dyes for different biomedical imaging applications.[6]

The second category comprises techniques that achieve super-resolution imaging by spatially modulating the excitation light to compress the point spread function (PSF) of the optical microscope system. Representative methods include stimulated emission depletion (STED) microscopy and reversible saturable optical linear fluorescence transitions (RSOLFT) microscopy.[7,8] STED is capable of super-resolution imaging, with a resolution range of 20–60 nm,[9,10] and a higher depletion laser power intensity corresponds to a higher spatial resolution. Additionally, it requires specific fluorescent dyes, which limits its application in live cell observations.[11,12] RSOLFT can reduce the optical power density of STED by eight orders of magnitude, by suppressing the luminescence of fluorescent molecules with switching effects in the annular spot region. However, this method also requires specific fluorescent dyes.[11,13,14]

The third category comprises frequency-mixing techniques, of which structured illumination microscopy (SIM) is the major type.[15,16] SIM uses streaked structured light to excite a sample to generate fluorescence, thus shifting undetectable high-frequency information to the optical system passband via the Moiré effect.[17–19] Super-resolution images can subsequently be reconstructed using a phase-shift reconstruction algorithm.[20] Additionally, this method does not require high peak illumination intensity or special dyes,[14,15,21–28] and because wide-field SIM has a higher imaging speed, it is more suitable for imaging living cells. However, the patterned structured illumination is susceptible to scattering of the sample, and its aberration might fail the reconstruction.[29,30]

Second harmonic generation (SHG) is a nonlinear light-scattering process, in which the second harmonic signal is the raw signal of the sample, and fluorescent staining is not required;[31–33] hence, biological samples are free from photochemical toxicity. SHG microscopic imaging is usually performed using near-infrared femtosecond laser excitation,[33–37] thus reducing the photodamage and photobleaching of biological samples. Only the sample at the focal point generates the SHG signal, which enables the high-quality three-dimensional (3D) imaging of thick samples. However, because SHG has a coherent PSF, the wide-field SHG-SIM cannot improve its resolution.[38] Recently, Urban *et al.* successfully implemented the point-scan SHG-SIM experimentally,[39] and Gregor *et al.* achieved SHG super-resolution imaging using image scanning microscopy,[40] which improved the resolution by approximately 2-fold, compared to conventional SHG microscopy. Our research group also proposed the point-scan SHG-SIM technique, which introduces the nonlinear effects of SHG and improves the resolution by approximately three-fold.[41] The point-scanning fringes, distinguished from wide-field methods, are generated through rather the spatio-temporal intensity modulation of the excitation laser than the optical interference in wide-field SIM. The point-scanning SHG-SIM technique can be performed on existing SHG microscopes by simply inserting a modulator between the laser and a commercial SHG microscopy to modulate laser intensity. Moreover, the point-scanning SIM technique can be directly used in other coherent nonlinear optical microscopes such as coherent anti-Stokes Raman (CARS) and so on.

Although we found that point and area detections affect the system resolution, a related analysis of the imaging performance of the two systems has not been conducted. Therefore, in this study, we systematically analyzed the influence of both detections on the resolution of SHG-SIM, simulated the corresponding imaging process by deriving the imaging equation, and performed experimental verification.

2. Materials and Methods

2.1. *Theory*

In a single-point scanning SIM, the intensity of the excitation beam is sinusoidally modulated by an

electro-optical modulator (EOM), and the sample is excited by the modulated excitation beam to emit signal light point-by-point via point scanning, thus realizing time-accumulated virtual fringed pattern illumination in the sample. The fringes interact with the sample structure and produce a Moiré mixing effect, transferring high-frequency information of the sample into the passband of the imaging system, which is then recorded by the detector and reconstructed using the SIM-reconstruction algorithm to produce super-resolution images. In this study, the raw SIM data obtained by the point and area detectors are different. For point detection, the signal light generated by each excited Airy spot on the sample constitutes one pixel of the raw SIM image. Conversely, for area detection, the signal light generated by each excited Airy spot on the sample produces a corresponding diffracted-image spot on the area detector. These spots are superimposed on each other to form a raw SIM image. Additionally, we theoretically derived an imaging process. The PSF in a microscopic imaging system is usually expressed as a first-order Bessel function of the first type.[42]

$$\mathrm{PSF}(x, y) = \left\{ \frac{2J_1\left(\frac{2\pi \mathrm{NA}}{\lambda}\sqrt{x^2 + y^2}\right)}{\frac{2\pi \mathrm{NA}\sqrt{x^2+y^2}}{\lambda}} \right\}^2, \quad (1)$$

where λ is the wavelength of the light, NA is the numerical aperture (NA) of the objective lens, J_1 is the first-order Bessel function, and (x, y) is the spatial coordinate system. When a laser beam is focused on the sample through the objective lens, the focused spot acts on the sample to obtain the following expression:

$$g_0(u, v; i, j) = S(u, v)h_{\mathrm{ex}}(u - i, v - j), \quad (2)$$

where S is the sample function, $h_{\mathrm{ex}} = \mathrm{PSF}(\lambda_{\mathrm{ex}})$ is PSFex, λ_{ex} are the excitation wavelengths, and the lower-right corner labels *ex* indicate the excitation; (u, v) is the coordinate system of the sample plane, and (i, j) is the coordinate system of the position of the excitation spot on the sample plane. When a point on the sample is excited and the resulting signal light is recorded by a detector, the Airy spot function is recorded as follows:

$$g_1(x, y; i, j) = \iint g_0(u, v; i, j)h_{\mathrm{em}}(x - u, y - v)dudv, \quad (3)$$

where $h_{\mathrm{em}} = \mathrm{PSF}(\lambda_{\mathrm{em}})$ is PSFem, λ_{em} are the emission wavelengths, and the lower-right corner labels

em indicate the emission, and (x, y) is the coordinate system of the detection surface. For a point scanning area detection (PS-AD) imaging system, the signal-light images corresponding to each excitation spot recorded by the array detector need to be summed to obtain a raw-signal light image, whose expression is as follows:

$$\begin{aligned} G(x, y) &= \iint g_1(x, y; i, j)didj \\ &= \iint \left\{ \iint [S(u, v)h_{\mathrm{ex}}(u - i, v - j)] \right. \\ &\quad \left. \times h_{\mathrm{em}}(x - u, y - v)dudv \right\}didj \\ &= \iint \left\{ \left[S(u, v)\iint h_{\mathrm{ex}(u-i,v-j)}didj \right] \right. \\ &\quad \left. h_{\mathrm{em}}(x - u, y - v) \right\}dudv \\ &= A \iint S(u, v)h_{\mathrm{em}}(x - u, y - v)dudv \\ &= A[S(x, y) \otimes h_{\mathrm{em}}(x, y)], \quad (4) \end{aligned}$$

where $A = \iint h_{\mathrm{ex}}(u - i, v - j)didj$ is a constant, and $\otimes$ is the convolution operation. Equation (4) shows that PSFem determines the imaging resolution of PS-AD, as in the case of wide-field imaging.

For point scanning point detection (PS-PD) imaging, each excitation Airy spot is integrated, and each integrated value is used as a single pixel of the raw-signal image. Subsequently, the integrated values are sorted according to the corresponding scanning order to reconstruct a raw-signal image, whose imaging equation can be written as follows:

$$\begin{aligned} G(i, j) &= \iint g_1(x, y; i, j)dxdy \\ &= \iint \left\{ \iint [S(u, v)h_{\mathrm{ex}}(u - i, v - j)] \right. \\ &\quad \left. \times h_{\mathrm{em}}(x - u, y - v)dudv \right\}dxdy \\ &= \iint \left\{ [S(u, v)h_{\mathrm{ex}}(u - i, v - j)] \right. \\ &\quad \left. \times \iint h_{\mathrm{em}}(x - u, y - v)dxdy \right\}dudv \\ &= B \iint S(u, v)h_{\mathrm{ex}}(u - i, v - j)dudv \\ &= B[S(i, j) \otimes h_{\mathrm{ex}}(i, j)], \quad (5) \end{aligned}$$

where $B = \iint h_{\mathrm{em}}(x - u, y - v)dxdy$ is a constant. Equation (5) shows that the imaging resolution of PS-PD is only dependent on PSFex.

The derivation of Eqs. (4) and (5) shows that the signal-detection processes of PS-AD and PS-PD are different, and that the imaging resolutions of both are affected by different factors. In a single-photon fluorescence imaging, the excitation wavelength is usually shorter than the emission wavelength; therefore, the full width at half maximum (FWHM) of PSFex is smaller than that of PSFem. Therefore, the imaging resolution of PS-PD was higher than that of PS-AD. However, in multiphoton fluorescence or SHG imaging, the FWHM of PSFex is usually larger than that of PSFem; therefore, PS-AD has a higher imaging resolution than PS-PD.

Furthermore, we can add structured lights to these two different imaging modalities to further improve the imaging resolution. In PS-AD linear SIM, the light field-intensity distribution of fluorescence in the sample is linearly related to the illumination-light field-intensity distribution; therefore, this imaging process is simplified into the following equation[30]:

$$D(r) = \{S(r)[I(r) \otimes h_{\mathrm{ex}}(r)]\} \otimes h_{\mathrm{em}}(r), \quad (6)$$

where $S(r)$ is the concentration of fluorescent molecules (characterizing the sample information), and $I(r)$ is the spatial modulation function of the structured light. The linear modulation function is expressed as follows:

$$I(r) = 1 + m\cos(2\pi k_0 r + \varphi), \quad (7)$$

where m is the modulation depth, k_0 is the frequency of the modulation function, and φ is the initial phase. The Fourier transform of the result calculated by substituting Eq. (7) into Eq. (6) is performed as follows:

$$\tilde{D}(k) = \mathcal{F}[\{S(r)[I(r) \otimes h_{\mathrm{ex}}(r)]\} \otimes h_{\mathrm{em}}(r)]$$

$$= \left\{ \tilde{S}(k) \otimes \begin{bmatrix} \delta(k)\tilde{H}_{\mathrm{ex}}(k) + \frac{m}{2}\delta(k - k_0) \\ \tilde{H}_{\mathrm{ex}}(k)e^{i\varphi} + \frac{m}{2}\delta(k + k_0) \\ \tilde{H}_{\mathrm{ex}}(k)e^{-i\varphi} \end{bmatrix} \right\} \tilde{H}_{\mathrm{em}}(k)$$

$$= \left\{ \tilde{S}(k) \otimes \begin{bmatrix} \delta(k)\tilde{H}_{\mathrm{ex}}(0) + \frac{m}{2}\delta(k - k_0) \\ \tilde{H}_{\mathrm{ex}}(k_0)e^{i\varphi} + \frac{m}{2}\delta(k + k_0) \\ \tilde{H}_{\mathrm{ex}}(-k_0)e^{-i\varphi} \end{bmatrix} \right\} \tilde{H}_{\mathrm{em}}(k)$$

$$= \left[\tilde{S}(k)\tilde{H}_{\mathrm{ex}}(0) + \frac{m}{2}\tilde{S}(k - k_0)e^{i\varphi}\tilde{H}_{\mathrm{ex}}(k_0) \right.$$
$$\left. + \frac{m}{2}\tilde{S}(k + k_0)e^{-i\varphi}\tilde{H}_{\mathrm{ex}}(-k_0) \right] \tilde{H}_{\mathrm{em}}(k)$$

$$= \tilde{S}_{\mathrm{Hem}}^{n}(k)\tilde{H}_{\mathrm{ex}}(0) + \frac{m}{2}\tilde{S}_{\mathrm{Hem}}^{p}(k - k_0)e^{i\varphi}\tilde{H}_{\mathrm{ex}}(k_0)$$
$$+ \frac{m}{2}S_{\mathrm{Hem}}^{v}(k + k_0)e^{-i\varphi}\tilde{H}_{\mathrm{ex}}(-k_0), \quad (8)$$

where k is the spatial frequency; δ is the impulse function; and $\tilde{S}$, $\tilde{H}_{\mathrm{ex}}$, and $\tilde{H}_{\mathrm{em}}$ are the Fourier transforms of S, h_{ex}, and h_{em}, respectively. $\tilde{S}_{\mathrm{Hem}}^{n}(k) = \tilde{S}(k)\tilde{H}_{\mathrm{em}}(k)$; $\tilde{S}_{\mathrm{Hem}}^{p}(k - k_0) = \tilde{S}(k - k_0)\tilde{H}_{\mathrm{em}}(k)$; $\tilde{S}_{\mathrm{Hem}}^{v}(k + k_0) = \tilde{S}(k + k_0)\tilde{H}_{\mathrm{em}}(k)$; $\tilde{S}_{\mathrm{Hem}}^{n}$ is the low-frequency information of the sample spectrum; and $\tilde{S}_{\mathrm{Hem}}^{p}$ and $\tilde{S}_{\mathrm{Hem}}^{v}$ represent the high-frequency spectral components of the sample. Therefore, the spectral information of the sample was extended, thereby improving the imaging resolution. The upper-right corner labels n, p, and v of $\tilde{S}_{\mathrm{Hem}}^{n}$, $\tilde{S}_{\mathrm{Hem}}^{p}$, and $\tilde{S}_{\mathrm{Hem}}^{v}$, respectively, represent the spectral components of the different frequency bands, and the lower-right corner label $H\mathrm{em}$ indicates that the spectrum is multiplied by the emission optical transfer function (OTF).

The imaging equation (Eq. (9)) is derived by modulating the intensity of the excitation light for PS-PD imaging, thereby modulating the high-frequency information, which cannot be collected, into low-frequency information that can pass through the passband of the imaging system[41]

$$D(i) = \iint S(u)I(u, i)h_{\mathrm{ex}}(u - i)h_{\mathrm{em}}(x - u)dudx$$

$$= \int h_{\mathrm{em}}(x - u)dx \int S(u)I(u, i)h_{\mathrm{ex}}(u - i)du$$

$$= C \int S(u)I(u, i)h_{\mathrm{ex}}(u - i)du$$

$$= C\{[S(i)I(i)] \otimes h_{\mathrm{ex}}(i) + I(i)[S(i) \otimes h_{\mathrm{ex}}(i)]\}, \quad (9)$$

where $I(u, i)$ is the sinusoidal modulation function[41] and $C = \int h_{\mathrm{em}}(x - u)dx$ is a constant. The expression of $D(i)$ is Fourier transformed as follows:

$$\tilde{D}(k) = \mathcal{F}[C\{[S(i)I(i)] \otimes h_{\mathrm{ex}}(i) + I(i)[S(i) \otimes h_{\mathrm{ex}}(i)]\}]$$
$$= C\{[\tilde{S}(k) \otimes \tilde{I}(k)]\tilde{H}_{\mathrm{ex}}(k) + \tilde{I}(k) \otimes [\tilde{S}(k)\tilde{H}_{\mathrm{ex}}(k)]\}$$
$$= C\left\{ \left[\tilde{S}_{\mathrm{Hex}}^{n}(k) + \frac{m}{2}\tilde{S}_{\mathrm{Hex}}^{p}(k - k_0)e^{i\varphi} \right. \right.$$

$$+\frac{m}{2}\tilde{S}^{v}_{H\text{ex}}(k+k_0)e^{-i\varphi}\Big]$$
$$+\Big[\tilde{S}^{n}_{H\text{ex}}(k)+\frac{m}{2}\tilde{S}^{n}_{H\text{ex}}(k-k_0)e^{i\varphi}$$
$$+\frac{m}{2}\tilde{S}^{n}_{H\text{ex}}(k+k_0)e^{-i\varphi}\Big]\Big\},$$

$$(10)$$

where $\tilde{D}(k)$ and $\tilde{H}_{\text{ex}}(k)$ are the Fourier transforms of $D(i)$ and $h_{\text{ex}}(i)$, respectively; $\tilde{S}^{n}_{H\text{ex}}(k) = \tilde{S}(k)\tilde{H}_{\text{ex}}(k)$, $\tilde{S}^{p}_{H\text{ex}}(k-k_0) = \tilde{S}(k-k_0)\tilde{H}_{\text{ex}}(k)$ and $\tilde{S}^{v}_{H\text{ex}}(k+k_0) = \tilde{S}(k+k_0)\tilde{H}_{\text{ex}}(k)$. Further, $\tilde{S}^{n}_{H\text{ex}}$ is the low-frequency information of the sample spectrum, while $\tilde{S}^{p}_{H\text{ex}}$ and $\tilde{S}^{v}_{H\text{ex}}$ represent the high-frequency spectral components of the sample. Therefore, the spectral information of the sample was extended, thereby improving the imaging resolution. The right subscripts $H\text{ex}$ of $\tilde{S}^{n}_{H\text{ex}}$, $\tilde{S}^{p}_{H\text{ex}}$, and $\tilde{S}^{v}_{H\text{ex}}$ indicate the product of the spectrum and OTF of the excitation.

From Eqs. (8) and (10), we can see that PS-AD and PS-PD in linear SIM can broaden the OTF passband to $[-k_c^{\text{em}}-k_0, +k_c^{\text{em}}+k_0]$ and $[-k_c^{\text{ex}}-k_0, +k_c^{\text{ex}}+k_0]$, respectively.

Here, we further discuss the effects of the two detection methods on the resolution under SHG-SIM conditions with optical nonlinear effects. Nonlinear optical effects arise when illuminating samples with noncentrosymmetric-ordered structures under intense lighting.[43]

$$P = \chi^{(1)}\cdot\vec{E} + \chi^{(2)}:\vec{E}\cdot\vec{E} + \chi^{(3)}\vdots\vec{E}\cdot\vec{E}\cdot\vec{E} + \cdots,$$

$$(11)$$

where $\chi^{(i)}$ is the optical magnetization rate, $\vec{E}$ is the distribution of the electric field, and the quadratic term $P^{(2)} = \chi^{(2)}:\vec{E}\cdot\vec{E}$ represents the SHG signal, which is proportional to the square of the excitation intensity and can be used to characterize the noncentrosymmetric-ordered structure of the sample. Therefore, there is $h_{\text{ex}} = \text{PSF}^2(\lambda_{\text{ex}})$ in the SHG system.

The PS-AD-based SHG-SIM (A-SHG-SIM) imaging equation is as follows:

$$\tilde{D}(k) = \mathcal{F}[\{S(r)[I^2(r)\otimes h_{\text{ex}}(r)]\}\otimes h_{\text{em}}(r)]$$
$$= \Big\{\tilde{S}(k)\otimes\Big[\Big(1+\frac{m^2}{2}\Big)\delta(k)\tilde{H}_{\text{ex}}(0)+m\delta(k-k_0)$$
$$\times\tilde{H}_{\text{ex}}(k_0)e^{i\varphi}+m\delta(k+k_0)\tilde{H}_{\text{ex}}(-k_0)e^{-i\varphi}$$

$$+\frac{m^2}{4}\delta(k-2k_0)\tilde{H}_{\text{ex}}(2k_0)e^{i2\varphi}$$
$$+\frac{m^2}{4}\delta(k+2k_0)\tilde{H}_{\text{ex}}(-2k_0)e^{-i2\varphi}\Big]\Big\}\tilde{H}_{\text{em}}(k)$$
$$=\Big(1+\frac{m^2}{2}\Big)\tilde{H}_{\text{ex}}(0)\tilde{S}^{n}_{H\text{em}}(k)+m\tilde{H}_{\text{ex}}(k_0)\tilde{S}^{p}_{H\text{em}}$$
$$\times(k-k_0)e^{i\varphi}+m\tilde{H}_{\text{ex}}(-k_0)\tilde{S}^{v}_{H\text{em}}(k+k_0)e^{-i\varphi}$$
$$+\frac{m^2}{4}\tilde{H}_{\text{ex}}(2k_0)\tilde{S}^{2p}_{H\text{em}}(k-2k_0)e^{i2\varphi}$$
$$+\frac{m^2}{4}\tilde{H}_{\text{ex}}(-2k_0)\tilde{S}^{2v}_{H\text{em}}(k+2k_0)e^{-i2\varphi},$$

$$(12)$$

where $\tilde{S}^{2p}_{H\text{em}}(k-2k_0) = \tilde{S}(k-2k_0)\tilde{H}_{\text{em}}(k)$, $\tilde{S}^{2v}_{H\text{em}}(k+2k_0) = \tilde{S}(k+2k_0)\tilde{H}_{\text{em}}(k)$, and $\tilde{S}^{2p}_{H\text{em}}$ and $\tilde{S}^{2v}_{H\text{em}}$ represent the high-frequency spectral components of the sample. The upper-right corner labels n, p and v of $\tilde{S}^{n}_{H\text{em}}$, $\tilde{S}^{p}_{H\text{em}}$, and $\tilde{S}^{v}_{H\text{em}}$ represent the spectral components of the different frequency bands. Because of the nonlinear SHG response, the imaged spectral information has additional $\tilde{S}^{2p}_{H\text{em}}(k-2k_0)$ and $\tilde{S}^{2v}_{H\text{em}}(k+2k_0)$ spectral components, compared to the PS-AD imaging of linear SIM, thus enabling the extension of the OTF passband of the SHG imaging system to $[-k_c^{\text{em}}-2k_0+k_c^{\text{em}}+2k_0]$ (k_c^{em} is the cut-off frequency of the emission OTF), while this $2k_0 \leq k_c^{\text{ex}}$ condition is required (k_c^{ex} is the cut-off frequency of the excitation OTF).

The PS-PD-based SHG-SIM (P-SHG-SIM) imaging equation is as follows:

$$\tilde{D}(k) = \mathcal{F}(C\{[S(i)I^2(i)]\otimes h_{\text{ex}}(i)$$
$$+I^2(i)[S(i)\otimes h_{\text{ex}}(i)]\})$$
$$= C\left\{\begin{bmatrix}\tilde{S}^{n}_{H\text{ex}}(k)+m\tilde{S}^{p}_{H\text{ex}}(k-k_0)e^{i\varphi}\\ +m\tilde{S}^{v}_{H\text{ex}}(k+k_0)e^{-i\varphi}\\ +\dfrac{m^2}{4}\tilde{S}^{2p}_{H\text{ex}}(k-2k_0)e^{i2\varphi}\\ +\dfrac{m^2}{4}\tilde{S}^{2v}_{H\text{ex}}(k+2k_0)e^{-i2\varphi}\end{bmatrix} + \begin{bmatrix}\tilde{S}^{n}_{H\text{ex}}(k)+m\tilde{S}^{n}_{H\text{ex}}(k-k_0)e^{i\varphi}\\ +m\tilde{S}^{n}_{H\text{ex}}(k+k_0)e^{-i\varphi}\\ +\dfrac{m^2}{4}\tilde{S}^{n}_{H\text{ex}}(k-2k_0)e^{i2\varphi}\\ +\dfrac{m^2}{4}\tilde{S}^{n}_{H\text{ex}}(k+2k_0)e^{-i2\varphi}\end{bmatrix}\right\},$$

$$(13)$$

where $\tilde{S}^{2p}_{H\mathrm{ex}}(k - 2k_0) = \tilde{S}(k - 2k_0)\tilde{H}_{\mathrm{ex}}(k)$; $\tilde{S}^{2v}_{H\mathrm{ex}}(k + 2k_0) = \tilde{S}(k + 2k_0)\tilde{H}_{\mathrm{ex}}(k)$. $\tilde{S}^{2p}_{H\mathrm{ex}}$ and $\tilde{S}^{2v}_{H\mathrm{ex}}$ represent the high-frequency spectral components of the sample. Compared with PS-PD imaging of linear SIM, the imaging spectrum was expanded with two spectral components: $\tilde{S}^{2p}_{H\mathrm{ex}}(k - 2k_0)$ and $\tilde{S}^{2v}_{H\mathrm{ex}}(k + 2k_0)$, thus enabling the extension of the OTF passband of the SHG imaging system to $[-k_c^{\mathrm{ex}} - 2k_0 + k_c^{\mathrm{ex}} + 2k_0]$, while this $k_0 \leq k_c^{\mathrm{ex}}$ condition is required.

Comparing A-SHG-SIM and P-SHG-SIM based on Eqs. (12) and (13), we can see that A-SHG-SIM and P-SHG-SIM can extend the OTF passband to $[-k_c^{\mathrm{em}} - 2k_0, +k_c^{\mathrm{em}} + 2k_0]$ and $[-k_c^{\mathrm{ex}} - 2k_0, +k_c^{\mathrm{ex}} + 2k_0]$, respectively.

2.2. *Simulation*

We simulated the imaging process of PS-PD and PS-AD using MATLAB (version 2018b). The microfilament-like samples were formed using discrete points (Fig. 1). The NA of the objective lens was set to 1.4, and three different groups of single-photon imaging conditions were set for PS-PD:

(1) $h_{\mathrm{ex}} = \mathrm{PSF}(\lambda_{\mathrm{ex}} = 488\,\mathrm{nm})$,
    $h_{\mathrm{em}} = \mathrm{PSF}(\lambda_{\mathrm{em}} = 550\,\mathrm{nm})$;

(2) $h_{\mathrm{ex}} = \mathrm{PSF}(\lambda_{\mathrm{ex}} = 405\,\mathrm{nm})$,
    $h_{\mathrm{em}} = \mathrm{PSF}(\lambda_{\mathrm{em}} = 550\,\mathrm{nm})$;
(3) $h_{\mathrm{ex}} = \mathrm{PSF}(\lambda_{\mathrm{ex}} = 405\,\mathrm{nm})$,
    $h_{\mathrm{em}} = \mathrm{PSF}(\lambda_{\mathrm{em}} = 650\,\mathrm{nm})$.

Figure 1 shows the PS-PD-simulated imaging results and a detailed corresponding matrix-simulated imaging procedure is provided in Appendix A.

In the PS-PD imaging mode, the simulation imaging resolution of Groups 1–3 is $178 \pm 3\,\mathrm{nm}$, $146 \pm 1\,\mathrm{nm}$, and $146 \pm 1\,\mathrm{nm}$, respectively. According to the theoretical equation of the PS-PD imaging resolution, $\varepsilon = 0.5\lambda_{\mathrm{ex}}/\mathrm{NA}$, the theoretical imaging resolutions in Figs. 1(b)–1(d) were calculated to be approximately $174\,\mathrm{nm}$, $145\,\mathrm{nm}$, and $145\,\mathrm{nm}$, respectively. This shows that the imaging resolution obtained from the simulation is consistent with theory. It can be concluded that the imaging resolution of PS-PD depends on $\mathrm{PSF}_{\mathrm{ex}}$ but not $\mathrm{PSF}_{\mathrm{em}}$, as derived from Eq. (5).

Three different groups of single-photon imaging conditions were set for PS-AD.

(1) $h_{\mathrm{ex}} = \mathrm{PSF}(\lambda_{\mathrm{ex}} = 488\,\mathrm{nm})$,
    $h_{\mathrm{em}} = \mathrm{PSF}(\lambda_{\mathrm{em}} = 650\,\mathrm{nm})$;
(2) $h_{\mathrm{ex}} = \mathrm{PSF}(\lambda_{\mathrm{ex}} = 488\,\mathrm{nm})$,
    $h_{\mathrm{em}} = \mathrm{PSF}(\lambda_{\mathrm{em}} = 550\,\mathrm{nm})$;
(3) $h_{\mathrm{ex}} = \mathrm{PSF}(\lambda_{\mathrm{ex}} = 405\,\mathrm{nm})$,
    $h_{\mathrm{em}} = \mathrm{PSF}(\lambda_{\mathrm{em}} = 550\,\mathrm{nm})$;
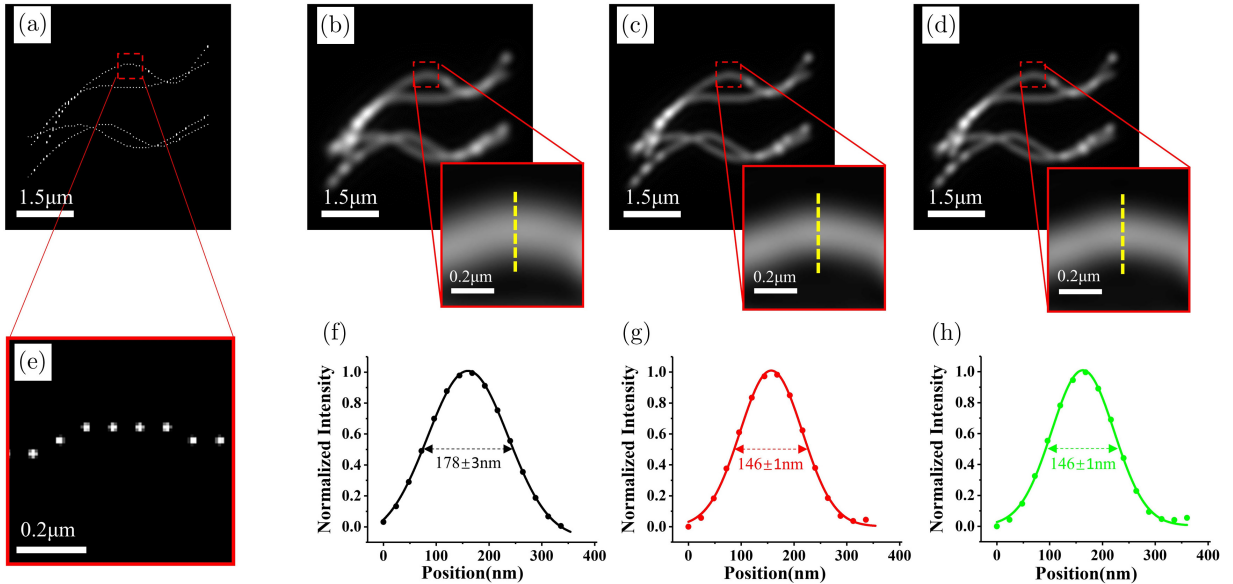

Fig. 1. PS-PD-simulated imaging results of three groups of different parameters; the original image of the sample and its partial enlarged view are shown in (a) and (e); (b)–(d) images corresponding to the three groups of parameters that are displayed from Group 1 to Group 3, respectively; (f)–(h) the intensity curves corresponding to the yellow dotted lines in the red blocks in (b)–(d), the average FWHM values are $178 \pm 3\,\mathrm{nm}$, $146 \pm 1\,\mathrm{nm}$, and $146 \pm 1\,\mathrm{nm}$, respectively.

Figure 2 shows the simulated imaging results of PS-AD; comparing these imaging conditions, PSFem of Group 2 is smaller than that of Group 1, and PSFex of Group 2 is larger than that of Group 3. In the PS-AD imaging mode, the simulation imaging resolution of Groups 1–3 is 233 ± 3 nm, 201 ± 4 nm, and 201 ± 4 nm, respectively. Therefore, it can be concluded that PSFex does not affect the imaging resolution of PS-AD. Thus, we can draw a conclusion that the PS-AD resolution is dependent on PSFem but not on PSFex. According to the PS-AD resolution equation, $\varepsilon = 0.5\lambda_{em}/NA$, the theoretical resolutions of Figs. 2(a)–2(c) are calculated to be 232 nm, 196 nm, and 196 nm, respectively. The simulation results are consistent with theory, thus confirming the derivation of Eq. (4). In conclusion, PSFem determines the imaging resolution of PS-AD, while the imaging resolution of PS-AD is not affected by PSFex.

The imaging processes of PS-PD and PS-AD were simulated. Owing to the SHG nonlinear process, the emission wavelength of SHG was exactly half of the excitation wavelength. To be consistent with the conditions in the following experiments, we used the excitation wavelength of 810 nm and the emission wavelength of 405 nm in the simulation.

The PSFex was $h_{ex} = PSF^2(\lambda_{ex} = 810$ nm), and the PSFem is $h_{em} = PSF(\lambda_{em} = 405$ nm). By combining the linear SIM with P-SHG and A-SHG for imaging, nonlinear structured light can be obtained in samples owing to the nonlinear effect of SHG imaging. Figure 3 shows the final simulated imaging results.

In the normal SHG imaging mode, the resolutions of P-SHG and A-SHG are 218 ± 3 nm and 148 ± 3 nm, respectively. The latter resolution is approximately 1.47-fold higher than that of the former. Stripes of 218 nm were loaded onto the sample of the P-SHG and A-SHG imaging systems. The four high-frequency spectral components of $\tilde{S}^p_{Hex}, \tilde{S}^v_{Hex}, \tilde{S}^{2p}_{Hex}$ and $\tilde{S}^{2v}_{Hex}$ of P-SHG-SIM and $\tilde{S}^p_{Hem}, \tilde{S}^v_{Hem}, \tilde{S}^{2p}_{Hem}$ and $\tilde{S}^{2v}_{Hem}$ of A-SHG-SIM were stitched with the fundamental frequency spectrum to obtain wider spectral information. In the SHG-SIM imaging mode, the simulation imaging resolutions of P-SHG-SIM and A-SHG-SIM are 114 ± 3 nm and 88 ± 3 nm, respectively.

2.3. *Optical system*

As shown in Fig. 4, a femtosecond titanium sapphire laser (MaiTai, Spectral Physics) with a pulse width of 100 fs was used, and the wavelength was
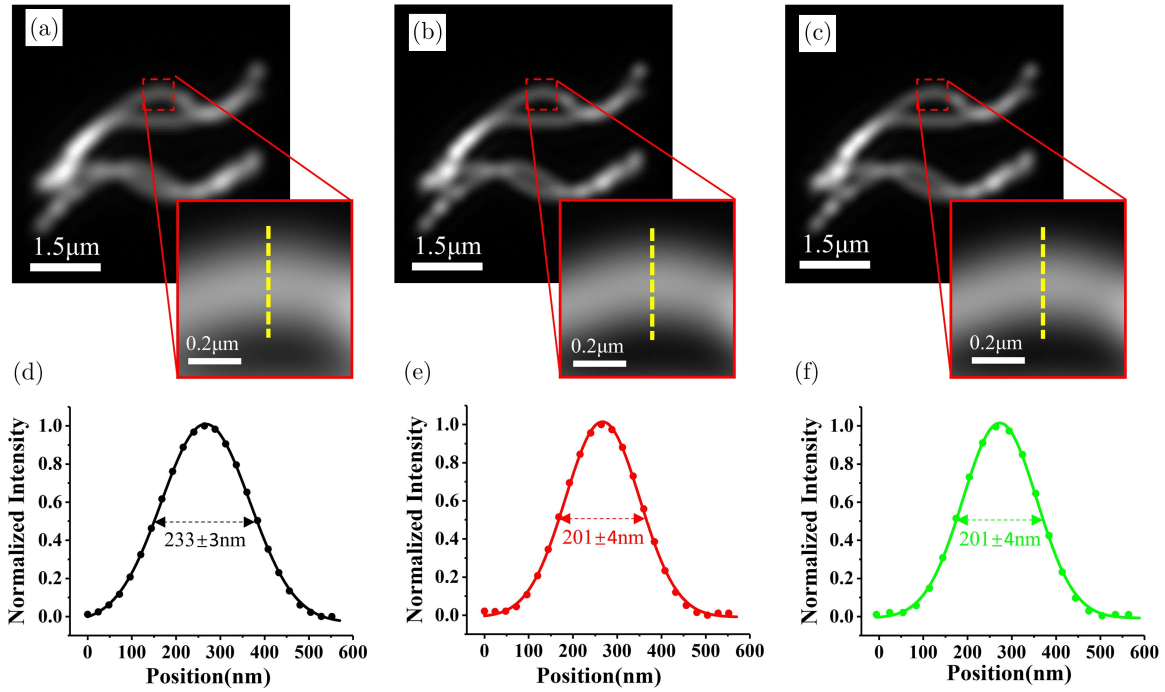

Fig. 2. Imaging results acquired by PS-AD of three groups of different parameters; (a)–(c) images corresponding to the three groups of parameters displayed from Group 1 to Group 3, respectively; (d)–(f) the intensity curves corresponding to the yellow dotted lines in the red blocks in (a)–(c), the average FWHM values are 233 ± 3 nm, 201 ± 4 nm, and 201 ± 4 nm, respectively.
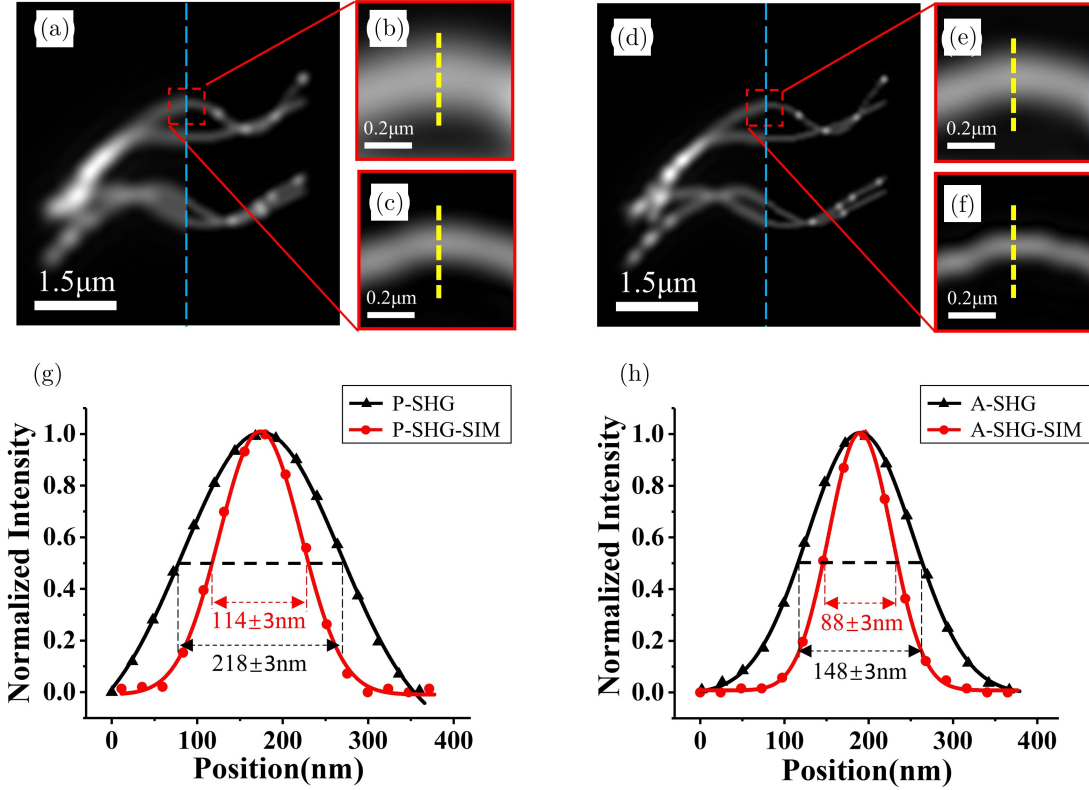
Fig. 3. Microfilament-like images obtained by P-SHG-SIM and A-SHG-SIM; (a) the left side is the conventional P-SHG image, and the right side is the P-SHG-SIM image; (b) and (c) are the local enlarged conventional P-SHG and P-SHG-SIM images of the red dashed box in (a), respectively; (d) the left side is the conventional A-SHG image, and the right side is the A-SHG-SIM image; (e) and (f) are the partially enlarged conventional A-SHG and A-SHG-SIM images of the red dashed box in (d), respectively; (g) and (h) correspond to the intensity curves of the yellow dotted line in the red box in (b)–(c) and (e)–(f), the average FWHM values are 218 ± 3 nm, 114 ± 3 nm, 148 ± 3 nm, and 88 ± 3 nm, respectively.

set to 810 nm. The laser passed through a half-wave plate (HWP, WPH05M-780, Thorlabs) and a polarization beamsplitter (PBS, CCM1-PBS251/M, Thorlabs); therefore, the intensity of the laser could be adjusted by the HWP. The PBS was placed after the HWP to obtain a higher purity of polarized light. Subsequently, the laser passed through the HWP and electro-optical modulator (EOM, EOM350, Conoptics). The HWP in front of the EOM was adopted to improve the EOM modulation efficiency. The laser then passed through a two-dimensional (2D) Galvo Scanner (2D GS, Model 6210H, Cambridge Tech), scanning lens (AC508-100-B, Thorlabs), tube lens (TL1, TTL200MP, Thorlabs), and objective lens (60×, NA 1.4 oil, Nikon), and it was then focused on the sample plane. The sample produced a second harmonic signal at the laser focus position, and the SHG signal was collected by the objective lens and passed through the tube lens (TL2, TTL200MP, Thorlabs), dichroic mirror filter (DMLP490, Thorlabs),

narrow bandpass filter (ET405/10, Chroma), zoom lens system (ZLS, NAVITAR), and finally reached the area detector array (sCMOS ZYLA 4.2, ANDOR). By turning reflector M2 in Fig. 4, the imaging optical path can be switched to point detector mode (PMT H7422-50, Hamamatsu).

Raster or snake-scanning mode is usually used for single-point scanning imaging. Figure 5 shows the scanning modalities for the raster and the snake. A snake-scan is used in PS-AD to avoid the disturbing signal excited in the return-scan path of the raster-scan (as shown in the scan path diagram in Fig. 5(b), bottom left, where the red dotted line represents the return-scan path). PS-PD uses a raster scanning approach. This is because when using a snake-scan approach for PS-PD imaging, it must be ensured that each scan point on the return trip aligns to the corresponding scan point on the return trip during the scanning process; otherwise, the final image was pixel-shifted, and the deflection accuracy of our 2D-GS did not meet this requirement.
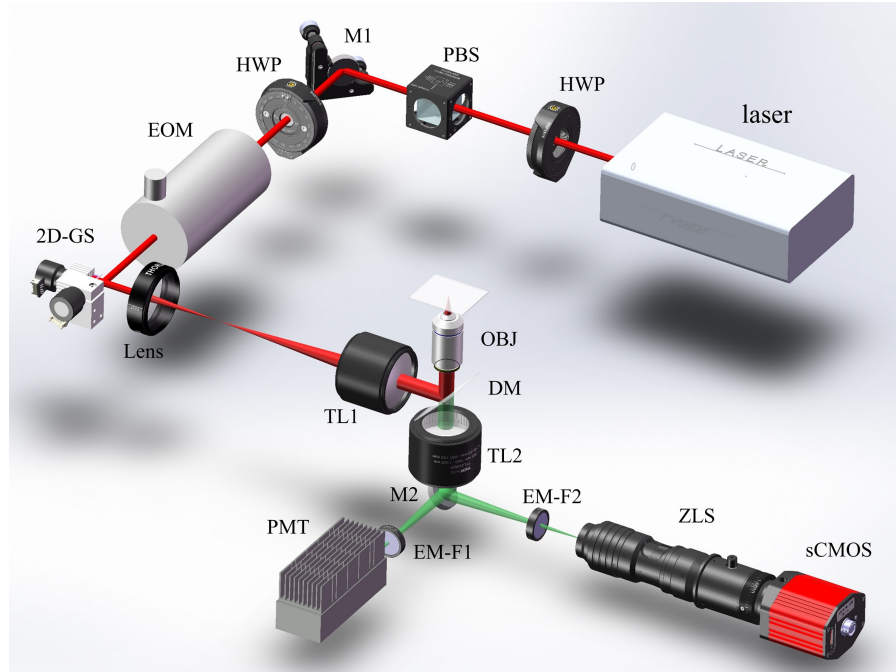
Fig. 4.   Single-point scanning SHG-SIM imaging system. HWP: Half-wave plate, PBS: Polarization beam splitter, M1, M2: Mirror 1, mirror 2, EOM: Electro-optical modulation, 2D-GS: Two-dimensional Galvo Scanner, TL1, TL2: Tube lens 1, tube lens 2, DM: Dichroic mirror, OBJ: Objective lens, EM-F1, EM-F2: emission filter 1, emission filter 2, ZLS: Zoom lens system, PMT: Photo-multiplier tube, and sCMOS: Scientific complementary metal oxide semiconductor.

In SHG-SIM, the EOM is synchronized with the galvo scanners. The final raw SIM data can be obtained after modulation, as shown in Fig. 6. Here, we removed the disturbing signal excited in the return-scan path of the raster-scan.

3.   Results

The object field of view (FOV) was $34 \times 34\,\mu\mathrm{m}^2$, and the number of scanning points was 800×800 (i.e., the number of imaging pixels of PS-PD); therefore, the imaging pixel size of PS-PD was

(a)	(b)

Fig. 5.   Scanning schematic diagrams of the snake and raster, (a) scanning method of the snake, and (b) scanning method of the raster.
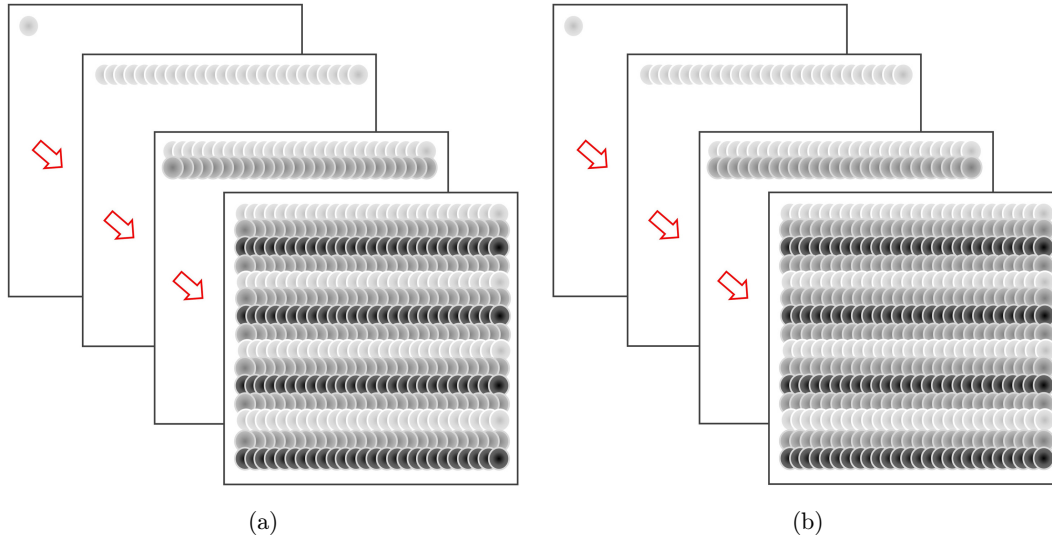
Fig. 6. Scanning schematic diagram of SIM employing the snake and raster modes: (a) Scanning process of SIM employing the snake mode and (b) scanning process of SIM employing the raster mode.

42.5 nm. For PS-AD, the imaging FOV can be changed by adjusting the zoom lens in front of the area detector; the individual pixel size of the final image was set to 21 nm in our experiment. The excitation wavelength of the experiment was 810 nm; the NA of the objective lens was 1.4; The dispersed nanoparticles of ZnO are imaged. The emission wavelength is 405 nm. A super-resolution image is reconstructured from 15 raw images for SHG-SIM. For the PS-PD and PS-AD system, the imaging speed is determined by the scanning speed. Therefore, the differences in imaging speed of PS-PD and PS-AD are nonsignificant. The acquisition time of each raw sinusoidal structured SHG illumination pattern was 2 s, and the exposure time of each excitation point in the sample is 12.5 μs.

Figure 7 shows the microscopy imaging results of the same area for P-SHG and A-SHG for the dispersed 50 nm ZnO particles. A-SHG has a higher resolution and can distinguish the two clusters of
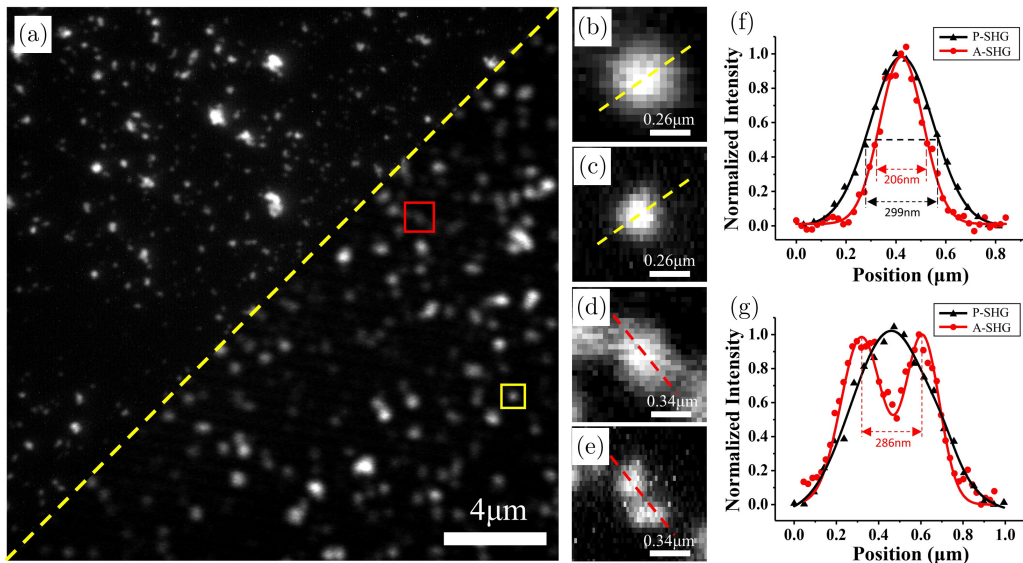

Fig. 7. Comparison of P-SHG and A-SHG of 50 nm ZnO nanoparticles; (a) ZnO nanoparticle images (bottom right: P-SHG; top left: A-SHG); (b) and (c) are partially enlarged images of the yellow box in (a), and (d) and (e) for the red box in (a), respectively. The results for P-SHG are displayed in (b) and (d). The results for A-SHG are displayed in (c) and (e). (f) is the normalized intensity plot of the yellow line in (b) and (c), and (g) is that of the red line in (d) and (e).
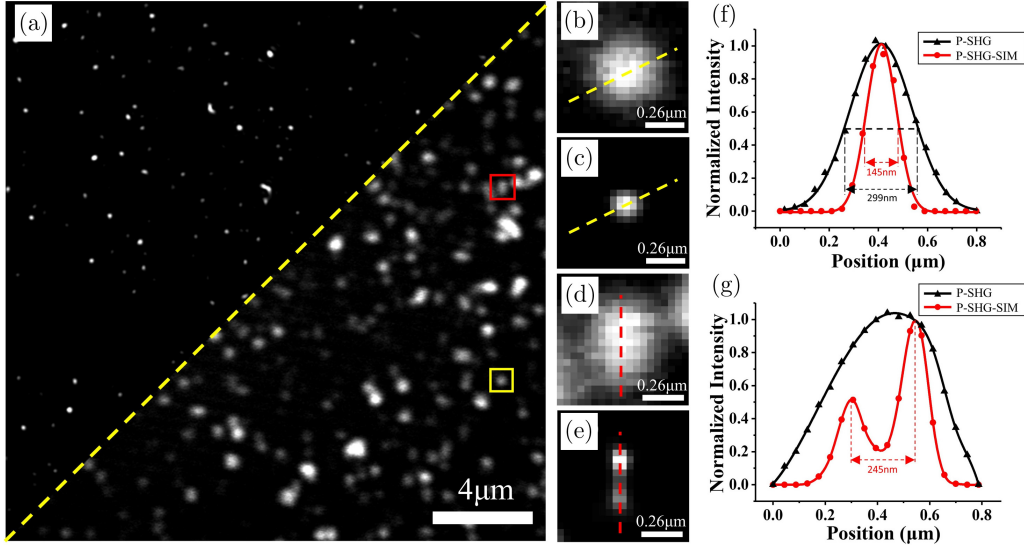
Fig. 8. Comparison of P-SHG and P-SHG-SIM imaging ZnO nanoparticles; (a) ZnO nanoparticles imaging (bottom right: P-SHG; top left: P-SHG-SIM); (b) and (c) are partially enlarged images of the yellow box in (a), and (d) and (e) for the red box in (a), respectively. The results for P-SHG are displayed in (b) and (d). The results for P-SHG-SIM are displayed in (c) and (e). (f) is the normalized intensity plot of the yellow line in (b) and (c), and (g) is that of the red line in (d) and (e).

ZnO particles, compared to P-SHG. The resolution of A-SHG calculated from Fig. 7(f) is 1.45 times higher than that of P-SHG, and the degree of resolution improvement is consistent with the value calculated from the simulated imaging (1.47 times). Therefore, both simulated imaging and experimental results validate the derivation of Eqs. (4) and (5). The residual sums of squares of the Fitting P-SHG versus Fitting A-SHG Gaussian fit curves in Figs. 7(f) and 7(g) were calculated to be (0.03352 versus 0.08017), and (0.00778 versus 0.05169), respectively. The sum of squared residuals of P-SHG is smaller than those of A-SHG, indicating that P-SHG has a better fit and thus better signal continuity than A-SHG.

To obtain a higher fringe frequency while obtaining a structured light modulation depth sufficient to reconstruct the super-resolution images, the periods of fringes were set to 292 nm based on the experimentally measured imaging resolutions of P-SHG and A-SHG. Therefore, according to the equation of the resolution improvement multiplier $m = (\varepsilon_T + \varepsilon)/\varepsilon_T (\varepsilon_T \leq \varepsilon)$, where ε_T is the period of fringes, it can be calculated that the resolution of both P-SHG and A-SHG can be improved by 2.0 times and 1.7 times in theory, respectively. In the experiment, the difference from linear SIM is that because of the nonlinear effect in SHG-SIM imaging,

the high-frequency spectrum of $(\tilde{S}^{2p}_{H\mathrm{ex}}\tilde{S}^{2v}_{H\mathrm{ex}})$ for P-SHG-SIM or $(\tilde{S}^{2p}_{H\mathrm{em}}\tilde{S}^{2v}_{H\mathrm{em}})$ for A-SHG-SIM that exceeds the cut-off frequency $(k_c + k_0)$ of the linear SIM is shifted into the OTF passband $(-k_c k_c)$ and passed through the imaging system and was thus recorded by the detector. When reconstructed, the high-frequency information components are shifted back to the correct positions, resulting in the required super-resolution images.[38]

Figure 8 shows the comparison of P-SHG and P-SHG-SIM. In Fig. 8(a), the P-SHG and P-SHG-SIM results are displayed in the lower-right corner and upper-left corner, respectively. The imaging resolution of P-SHG is 299 nm, and that of P-SHG-SIM is 145 nm. According to Fig. 8(g), P-SHG-SIM can distinguish two clusters of ZnO particles 245 nm apart, while P-SHG cannot.

Figure 9 shows the comparison of A-SHG and A-SHG-SIM. In Fig. 9(a), the A-SHG and A-SHG-SIM results are displayed in the lower-right corner and upper-left corner, respectively. As shown in Fig. 9(f), the FWHM of the A-SHG and A-SHG-SIM curves are 206 nm and 108 nm, respectively. Compared with A-SHG, A-SHG-SIM can distinguish two clusters of ZnO particles 141 nm apart. Figures 8 and 9 are the results for imaging the same area of the same sample with different imaging modes.
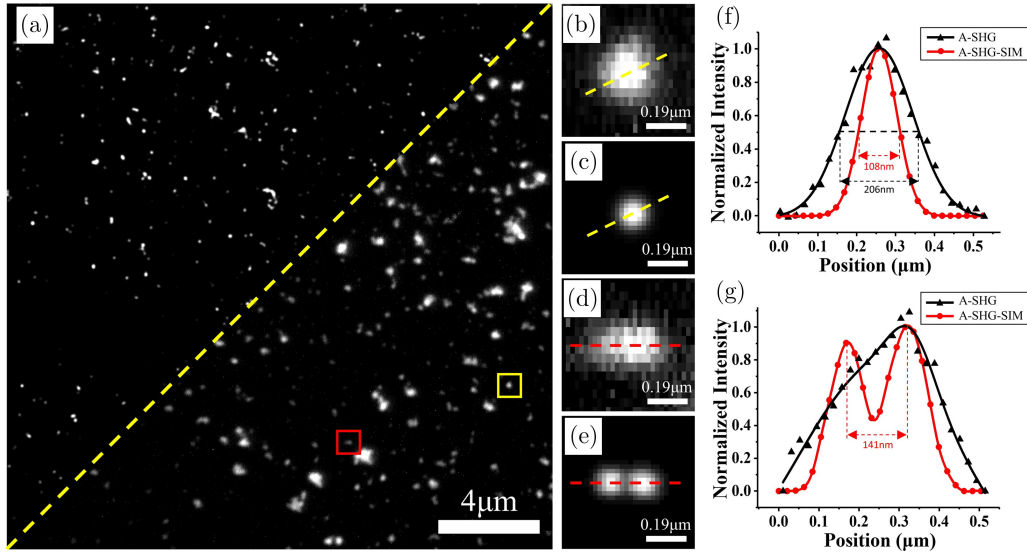
Fig. 9. Comparison of A-SHG and A-SHG-SIM imaging ZnO nanoparticles. (a) ZnO nanoparticles imaging (top left: A-SHG; bottom right: A-SHG-SIM); (b) and (c) partially enlarged images of the yellow box in (a), and (d) and (e) for the red box in (a). The results for A-SHG are displayed in (b) and (d). The results for A-SHG-SIM are displayed in (c) and (e). (f) is the normalized intensity plot of the yellow line in (b) and (c), and (g) is that of the red line in (d) and (e).

4. Discussion

Point-scanning SHG-SIM technique has the following advantages: (1) It can be performed on existing SHG microscopes by simply inserting a modulator between the laser and a commercial SHG microscopy to modulate laser intensity; (2) It can be used with excitation light intensity on the order of conventional SHG microscopes; (3) The super-resolution technique can be directly used in two photon fluorescence microscopy without specific fluorophores, and even in other coherent nonlinear optical microscopes such as coherent anti-Stokes Raman (CARS) and so on.

5. Conclusions

In this paper, we analyzed the distinction between point detection and area detection modes in single-point scanning imaging systems. The experimental results are in agreement with the simulated imaging results based on the derived equations. In SHG imaging, P-SHG imaging provides better continuity of detail, while A-SHG imaging provides a higher resolution; therefore, both imaging modalities have their own advantages. The combination of SIM with P-SHG and A-SHG imaging techniques exploits the light-slicing capability of SHG imaging to reduce out-of-focus signals, and it exploits the nonlinear

excitation effect to obtain nonlinear structured light, thus enabling nonlinear SIM. The final image resolutions that were obtained experimentally, with P-SHG-SIM and A-SHG-SIM had resolutions of 145 nm and 108 nm, respectively. The P-SHG-SIM and A-SHG-SIM imaging techniques can be applied to the biological samples.

Moreover, P-SHG-SIM can be selected to achieve a high resolution with better continuity of detail. As far as we know, continuity is helpful for pathological diagnosis. For example, when observing the pathological tissue of canceration, we can evaluate whether the tissue is invaded by cancer cells by judging whether the collagen is broken or not. A-SHG-SIM has a higher imaging resolution and dynamic range, which are beneficial for observing more distribution details of biological tissue structures. However, the structured light projected onto the sample in this experiment was limited by PSFex. The higher the modulation frequency of the structured light, the lower the weighting of the high-frequency information in the final image, thus making it more difficult to reconstruct the super-resolution image, which also results in a lower contrast in the final sample details.[44] Therefore, by combining the third harmonic with SIM technology, higher modulation frequencies of nonlinear structured light can be obtained with lower modulation frequencies of structured light, leading to a higher

weighting of the high-frequency information obtained. Thus, there is a higher contrast and more continuous detail in the reconstructed super-resolution image. The scattering in samples will reduce the signal-to-noise ratio of the fringes. When the confocal optical path and more sensitive detectors, such as Hybrid Photodetector (HPD), are used, the scattering noise can be suppressed. To improve the imaging speed, we expect the use of resonant scanners or multifocal excitation schemes in the future.

Acknowledgments

Conflicts of Interest

The authors have no conflicts of interest relevant to this article.

Appendix A

The following are the schematic diagrams of the simulated imaging for PS-PD and PS-AD.

Figure A.1 shows a schematic diagram of imaging a single-point laser-scan sample and convolving it with PSFem. Figure A.2 shows a schematic diagram of matrixed imaging for PS-PD. Figure A.3
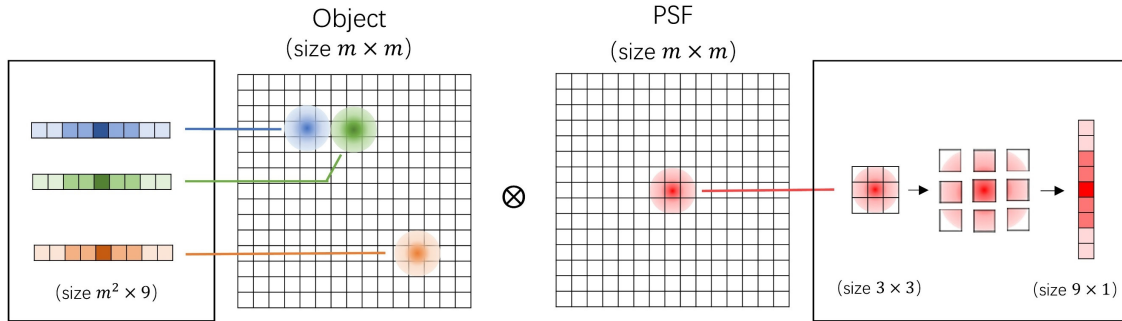

Fig. A.1.   Blue, green, and orange dots in the object indicate that the sample is excited by a scanning laser, and each excited dot is convolved with PSF to obtain the light intensity imaged on the detector. When each scanned and exciting point (that is, the element of the matrix) is rearranged in the sample as a column vector, the three exciting points of blue, green, and orange dots are rearranged to obtain the three column vectors of the left image; Conversion of the PSF element of the detection matrix into a row vector to result in the row vector of 9×1 shown in the right figure.
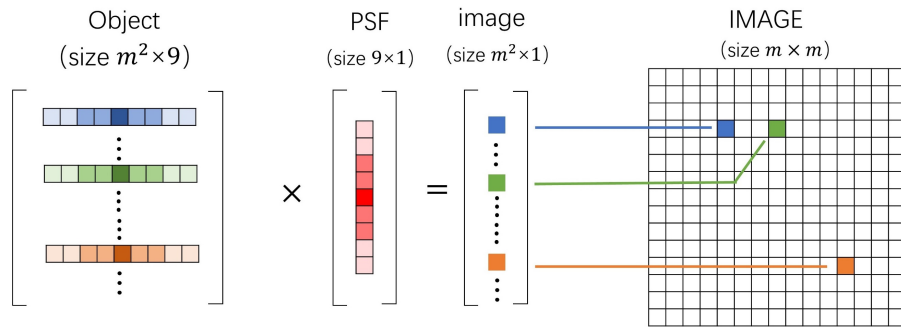

Fig. A.2.   Spot scan-point detection imaging; the matrix of rearrangement of samples in Fig. A.2 is integrated into the object matrix of $m^2 \times 9$ multiplied by the row vector PSF to obtain the image of the row vector of $m^2 \times 1$, and subsequently, it is rearranged as an $m \times m$ image matrix.
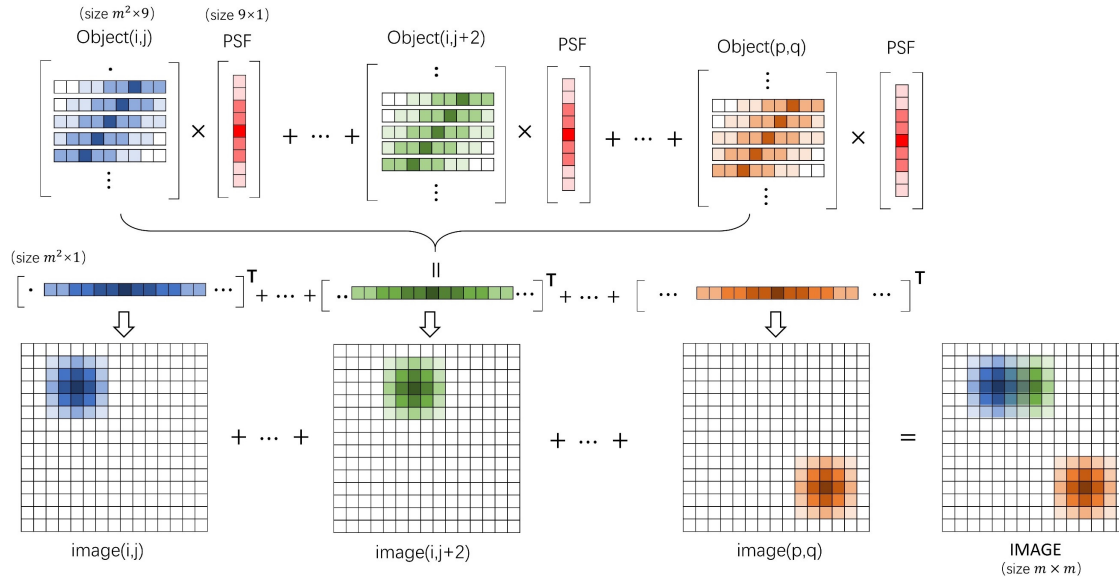
Fig. A.3. Point scan-area detection imaging; objects (i,j), $(i,j+2)$, and (p,q) in the figure indicate that the sample matrix is rearranged when the scanning points are in different positions and multiplied by the row. The vector PSF gets the $m \times m$ row vector and then rearranges the product row vector back to the $m \times m$ image (i,j), image $(i,j+2)$, and image (p,q). Finally, all scans are added to each image to obtain the IMAGE.

shows a schematic diagram of matrixed imaging for PS-AD.

References

1. S. T. Hess, T. P. Girirajan, M. D. Mason, "Ultra-high resolution imaging by fluorescence photo-activation localization microscopy," *Biophys. J.* **91**(11), 4258–4272 (2006).

2. B. Huang, W. Wang, M. Bates, X. Zhuang, "Three-dimensional super-resolution imaging by stochastic optical reconstruction microscopy," *Science* **319**(5864), 810–813 (2008).

3. E. Betzig, G. H. Patterson, R. Sougrat, O. W. Lindwasser, S. Olenych, J. S. Bonifacino, M. W. Davidson, J. Lippincott-Schwartz, H. F. Hess, "Imaging intracellular fluorescent proteins at nanometer resolution," *Science* **313**(5793), 1642–1645 (2006).

4. M. Pfender, N. Aslam, G. Waldherr, P. Neumann, J. Wrachtrup, "Single-spin stochastic optical reconstruction microscopy," *Proc. Natl. Acad. Sci. USA* **111**(41), 14669–14674 (2014).

5. A. H. Hainsworth, S. Lee, P. Foot, A. Patel, W. W. Poon, A. E. Knight, "Super-resolution imaging of subcortical white matter using stochastic optical reconstruction microscopy (STORM) and super-resolution optical fluctuation imaging (SOFI)," *Neuropathol. Appl. Neurobiol.* **44**(4), 417–426 (2018).

6. J. Tang, A. Vaziri, J. Akerboom, L. Looger, C. Shank, "Three dimensional super resolution fluorescence imaging of single bacterial cells by stereo photoactivated localization microscopy," *Microsc. Microanal.* **15**(S2), 564–565 (2009).

7. S. W. Hell, J. Wichmann, "Breaking the diffraction resolution limit by stimulated emission: Stimulated-emission-depletion fluorescence microscopy," *Opt. Lett.* **19**(11), 780–782 (1994).

8. S. W. Hell, "Far-field optical nanoscopy," *Abs. Pap. Am. Chem. Soc.* **238**(5828), 1153–1158 (2007).

9. Y. Silani, F. Hubert, V. M. Acosta, "Stimulated emission depletion microscopy with diamond silicon vacancy centers," *ACS Photon.* **6**(10), 2577–2582 (2019).

10. Z. Wu, X. Xu, P. Xi, "Stimulated emission depletion microscopy for biological imaging in four dimensions: A review," *Microsc. Res. Tech.* **84**(9), 1947–1958 (2021).

11. R. Sharma, M. Singh, R. Sharma, "Recent advances in STED and RESOLFT super-resolution imaging techniques," *Spectrochim. Acta A. Mol. Biomol. Spectrosc.* **231**, 117715 (2020).

12. H. Zhang, M. Zhao, L. Peng, "Nonlinear structured illumination microscopy by surface plasmon enhanced stimulated emission depletion," *Opt. Exp.* **19**(24), 24783–24794 (2011).

13. T. Grotjohann, I. Testa, M. Reuss, T. Brakemann, C. Eggeling, S. W. Hell, S. Jakobs, "rsEGFP2 enables fast RESOLFT nanoscopy of living cells," *Elife* **1**, e00248 (2012).

14. J. T. Frohn, H. F. Knapp, A. Stemmer, "True optical resolution beyond the Rayleigh limit achieved by standing wave illumination," *Proc. Natl. Acad. Sci. USA* **97**(13), 7232–7236 (2000).

15. H. Rainer, G. C. Christoph, "Laterally modulated excitation microscopy: Improvement of resolution by using a diffraction grating," *Proc. SPIE* **3568**, 185–196 (1999).

16. M. Gustafsson, D. Agard, J. Sedat, "Doubling the lateral resolution of wide-field fluorescence microscopy using structured illumination," *Proc. SPIE Int. Soc. Opt. Eng.* **3919**, 141–150 (2000).

17. L. Y. Xu, Y. W. Zhang, S. Lang, H. W. Wang, H. J. Hu, J. K. Wang, Y. Gong, "Structured illumination microscopy based on asymmetric three-beam interference," *J. Innov. Opt. Health Sci.* **14**(2), 2050027 (2021).

18. Y. L. Yu, J. N. Yu, Z. L. Huang, F. L. Zhou, "Application of super-resolution fluorescence microscopy in hematologic malignancies," *J. Innov. Opt. Health Sci.* **15**(2), 2230005 (2022).

19. M. T. Wang, L. Wang, X. M. Zheng, J. Zhou, J. J. Chen, Y. J. Zeng, J. L. Qu, Y. H. Shao, B. Z. Gao, "Nonlinear scanning structured illumination microscopy based on nonsinusoidal modulation," *J. Innov. Opt. Health Sci.* **14**(5), 2142002 (2021).

20. Z. Wang, T. Zhao, H. Hao, Y. Cai, K. Feng, X. Yun, Y. Liang, S. Wang, Y. Sun, P. R. Bianco, K. Oh, M. Lei, "High-speed image reconstruction for optically sectioned, super-resolution structured illumination microscopy," *Adv. Photon.* **4**(2), 026003 (2022).

21. E. H. Rego, L. Shao, J. J. Macklin, L. Winoto, G. A. Johansson, N. Kamps-Hughes, M. W. Davidson, M. G. Gustafsson, "Nonlinear structured-illumination microscopy with a photoswitchable protein reveals cellular structures at 50-nm resolution," *Proc. Natl. Acad. Sci. USA* **109**(3), E135–E143 (2012).

22. M. G. Gustafsson, "Nonlinear structured-illumination microscopy: Wide-field fluorescence imaging with theoretically unlimited resolution," *Proc. Natl. Acad. Sci. USA* **102**(37), 13081–13086 (2005).

23. R. Heintzmann, T. M. Jovin, C. Cremer, "Saturated patterned excitation microscopy—a concept for optical resolution improvement," *J. Opt. Soc. Am. A Opt. Image Sci. Vis.* **19**(8), 1599–1609 (2002).

24. H. Liisa, M. Ondrej, W. Kai, H. Rainer, "Structured illumination microscopy using photoswitchable fluorescent proteins," *Proc. SPIE* **6861**, 68610L (2008).

25. M. G. Gustafsson, L. Shao, P. M. Carlton, C. J. Wang, I. N. Golubovskaya, W. Z. Cande, D. A. Agard, J. W. Sedat, "Three-dimensional resolution doubling in wide-field fluorescence microscopy by structured illumination," *Biophys. J.* **94**(12), 4957–4970 (2008).

26. T. J. Lambert, J. C. Waters, "Navigating challenges in the application of superresolution microscopy," *J. Cell Biol.* **216**(1), 53–63 (2016).

27. Y. Wu, H. Shroff, "Faster, sharper, and deeper: Structured illumination microscopy for biological imaging," *Nat. Meth.* **15**(12), 1011–1019 (2018).

28. G. Vicidomini, P. Bianchini, A. Diaspro, "STED super-resolved microscopy," *Nat. Meth.* **15**(3), 173–182 (2018).

29. Z. Li, J. Hou, J. Suo, C. Qiao, L. Kong, Q. Dai, "Contrast and resolution enhanced optical sectioning in scattering tissue using line-scanning two-photon structured illumination microscopy," *Opt. Exp.* **25**(25), 32010–32020 (2017).

30. B. E. Urban, J. Yi, S. Chen, B. Dong, Y. Zhu, S. H. DeVries, V. Backman, H. F. Zhang, "Super-resolution two-photon microscopy via scanning patterned illumination," *Phys. Rev. E Stat. Nonlin. Soft Matter Phys.* **91**(4), 042703 (2015).

31. G. Xi, L. Qiu, S. Xu, W. Guo, F. Fu, D. Kang, L. Zheng, J. He, Q. Zhang, L. Li, C. Wang, J. Chen, "Computer-assisted quantification of tumor-associated collagen signatures to improve the prognosis prediction of breast cancer," *BMC Med.* **19**(1), 273 (2021).

32. L. Qiu, D. Kang, C. Wang, W. Guo, F. Fu, Q. Wu, G. Xi, J. He, L. Zheng, Q. Zhang, X. Liao, L. Li, J. Chen, H. Tu, "Intratumor graph neural network recovers hidden prognostic value of multi-biomarker spatial heterogeneity," *Nat. Commun.* **13**(1), 4250 (2022).

33. H. Hirayama, M. Watai, "Two-photon resonance in optical second harmonic generation from quantum well states in ultra-thin Ag films grown on Si(1 1 1) surfaces," *Surf. Sci.* **600**(18), 3825–3829 (2006).

34. J. Adur, V. B. Pelegati, A. A. D. Thomaz, F. Bottcher-Luiz, L. A. L. A. Andrade, D. B. Almeida, H. F. Carvalho, C. L. Cesar, "Combined nonlinear laser imaging (two-photon excitation fluorescence, second and third-harmonic generation, and fluorescence lifetime imaging microscopies) in ovarian tumors," *Proc. SPIE* **8226**, 82261A (2012).

35. R. M. Williams, W. R. Zipfel, W. W. Webb, "Interpreting second-harmonic generation images of collagen I fibrils," *Biophys J.* **88**(2), 1377–1386 (2005).

36. W. R. Zipfel, R. M. Williams, R. Christie, A. Y. Nikitin, B. T. Hyman, W. W. Webb, "Live tissue intrinsic emission microscopy using multiphoton-excited native fluorescence and second harmonic generation," *Proc. Natl. Acad. Sci. USA* **100**(12), 7075–7080 (2003).

37. N. H. Green, R. M. Delaine-Smith, H. J. Askew, R. Byers, G. C. Reilly, S. J. Matcher, "A new mode of contrast in biological second harmonic generation microscopy," *Sci. Rep.* **7**(1), 13331 (2017).

38. K. Wicker, R. Heintzmann, "Resolving a misconception about structured illumination," *Nat. Photon.* **8**(5), 342–344 (2014).

39. B. E. Urban, B. Dong, X. Zhang, H. Yang, H. F. Zhang, "Patterned-illumination second harmonic generation microscopy of collagen fibrils in rat scleras," *Opt. Lett.* **43**(21), 5190–5193 (2018).

40. I. Gregor, M. Spiecker, R. Petrovsky, J. Grosshans, R. Ros, J. Enderlein, "Rapid nonlinear image scanning microscopy," *Nat. Meth.* **14**(11), 1087–1089 (2017).

41. L. Wang, X. Zheng, J. Zhou, M. Wang, J. Chen, Y. Zeng, G. Xu, Y. Wang, H. Qiu, Y. Shao, J. Qu, B. Z. Gao, Y. Gu, "Improvement in resolution of multiphoton scanning structured illumination microscopy via harmonics," *Engineering* **16**, 65–72 (2022).

42. C. J. R. Sheppard, M. Gu, "Image formation in two-photon fluorescence microscopy," *Optik Int. J. Light Electron Opt.* **86**(3), 104–106 (1990).

43. R. W. Boyd, The nonlinear optical susceptibility, *Nonlinear Optics*, R. W. Boyd, Eds., pp. 1–64, Academic Press, United States, Cambridge, Massachusetts (2020).

44. C. H. Yeh, C. Z. Tan, C. A. Cheng, J. T. Hung, S. Y. Chen, "Improving resolution of second harmonic generation microscopy via scanning structured illumination," *Biomed. Opt. Exp.* **9**(12), 6081–6090 (2018).